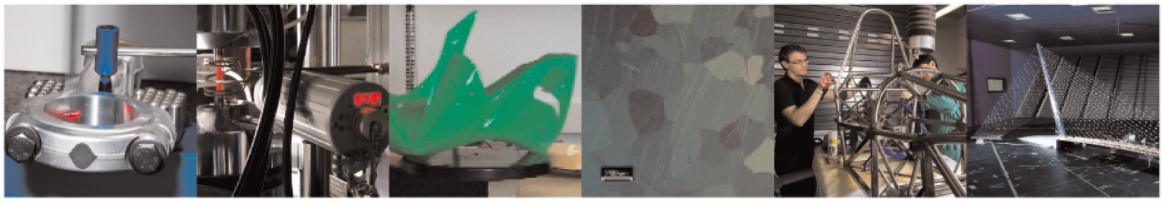

Synthesis of KNN powders: scaling effect of the milling step

Ruben Beltrami, Elisa Mercadelli, Carlo Baldisserri, Carmen Galassi, Francesco Braghin and Nora Lecis

This is a post-peer-review, pre-copyedit version of an article published in Powder Technology. The final authenticated version is available online at: http://dx.doi.org/j.powtec.2020.07.098

DIPARTIMENTO DI MECCANICA ■ POLITECNICO DI MILANO
via G. La Masa, 1 ■ 20156 Milano ■ EMAIL (PEC): pecmecc@cert.polimi.it
http://www.mecc.polimi.it
Rev. 0

Synthesis of KNN powders: scaling effect of the milling step

Ruben Beltrami[a], Elisa Mercadelli[b*], Carlo Baldisserri[b], Carmen Galassi[a,b], Francesco Braghin[a] and Nora Lecis[a]

[a] Department of Mechanical Engineering, Politecnico di Milano, Milan, Italy

[b] CNR-ISTEC, Istituto di Scienza e Tecnologia dei Materiali Ceramici, Faenza, Italy

*Corresponding Author; Phone: +39 0546 699743, Fax: +390546 46381 e-mail: elisa.mercadelli@istec.cnr.it

Abstract

The scaled-up production of lead-free potassium sodium niobate (KNN)-based piezoceramics still suffers from poor reliability and reproducibility issues that hinder their penetration into the piezoelectric market. To address this issue, pure KNN ceramics were prepared in this work by mechanochemical activation of the powders, obtaining high density sintered pellets featuring fine and uniform-grain-size. Results show that both cumulative kinetic energy released in the system and hindrance factor, the latter being paramount, must be properly taken into account when the synthesis is scaled-up. Mechanochemical activation strongly effects both stoichiometry and morphology of the final KNN powders during the milling step, which in turn effects the piezoelectric properties of the sintered pellets. Results from this work indicate that proper design and control of the powder synthesis process is a valuable tool in the scaled-up production of KNN powders for the production of reliable and performant KNN ceramics.

Keywords

$(K_{0.5}Na_{0.5})NbO_3$; Lead-free; Mechanochemical powder-activation; Microstructure; Ferroelectricity; Piezoelectricity

1. Introduction

Due to their remarkable piezoelectric properties, KNN-based lead-free ceramics have emerged in recent years as the most promising candidates to replace lead-based materials. Suitably doped KNN-based piezoceramics were found to display strong electromechanical coupling in the intermediate and low-temperature regime (25°C–200°C), with d_{33} values ranging between 350 and 700 pC/N, i.e. comparable to those of soft commercial PZT piezoceramics [1-3]. Several practical applications have been explored, including piezoelectric actuators, piezoelectric transformers, and piezoelectric energy harvesters [4-8]. However, poor sinterability and weak reproducibility of functional properties still hinder extensive applications of KNN-based materials.

Processing-related problems have been singled out as the main reason preventing widespread exploitation of KNN piezoceramics. Specifically, a narrow sintering range close to the 1140°C solidus temperature renders the sintering of KNN ceramic bodies problematic, making it difficult to obtain high-density KNN piezoceramics at lower sintering temperatures without the use of additives. Use of sacrificial powders to control the sintering atmosphere and hinder the loss of volatile species is a feasible approach for promoting densification and modulating the microstructure [9]. Another critical issue is alkali loss, which may occur both in the initial processing stages involving manipulation of humidity-sensitive alkaline reagents, and during solid-state synthesis by HT alkali volatilization [10, 11]. Non-homogeneous distribution of Nb and differing diffusion rates of sodium and potassium ions may contribute to local heterogeneities, wrong stoichiometry, and presence of unwanted secondary phases in KNN-materials prepared by conventional solid-state reaction, all of which leading to poorly reproducible functional properties. Additionally, particle coarsening often takes place during synthesis, which in turn diminishes the sinterability of the resulting powder and weakens the piezoelectric response.

These problems could be overcome by pre-reacting B-site ions or, alternatively, by mechanochemical activation of the reagent mixture [12-15]. Rojac et al. explored in detail mechanochemical activation and synthesis of alkaline niobate ceramics systems [16-18]. The high-energy ball milling process causes cumulative kinetic energy to reach the energetic barrier in order to activate the reaction [19], decreasing the calcination temperature and allowing controlling and preventing volatilization of alkaline species. Mechanochemical activation affords significant advantages, chiefly shorter synthesis times and

reduced volatilization of alkaline species. Furthermore, enhanced chemical homogeneity with improved crystal structure of synthesized powder is achieved [20, 21].

However, taking lead-free KNN materials to industrial-scale production while keeping strictly reproducible powder morphology and final microstructure; conserving reliable and reproducible piezoelectric performance, and keeping production costs low by performing short and efficient milling and operating at low calcination and densification temperatures, remains an open issue.

This work is focused on two key steps in the solid-state synthesis of the powders, i.e. milling before and after calcination, both of which critical in the scale-up of the batch size. Two batches of $(K_{0.5}Na_{0.5})NbO_3$ (KNN) powder were prepared via a mechanochemical-assisted activation method using a planetary milling system and controlling the mixing/milling conditions. The cumulative kinetic energy (ΔE_{cum}) was estimated for both batches, and correlated with the morphology of the resulting powders and the microstructure of the corresponding sintered KNN pellets, which were found to lead to different piezoelectric performance.

2. Material and methods

2.1. Solid-state synthesis of KNN

Powders of the nominal composition $(K_{0.5}Na_{0.5})NbO_3$ were synthesized using the mechanochemical activation-assisted route. K_2CO_3 (Merck, purity 99%), Na_2CO_3 (Merck, purity 99.5%) and Nb_2O_5 (Aldrich, purity 99.99%, average particle size ≤ 45 μm) powders were used as raw materials; after drying at 80°C for 24 hours they were weighed according to the requested stoichiometry.

Two main batches were synthetized: batch 1 (KNN1, 35 g) and batch 2 (KNN2, 70 g). The powders were mixed in a Fritsch Planetary Mill (PULVERISETTE 6), in distilled water, in air, in a zirconia jar (volume 250 cm^3) with spherical zirconia milling media (2 mm diameter) in 8:1 (batch 1) and 6:1 (batch 2) balls-to-powder weight ratios. The high-energy ball milling routine, lasting 100 min. at 600 rpm rotation speed, was programmed in such a way that the rotation of the sun wheel and jar reversed every 2 min, with a rest interval of 8 min to avoid excessive heating.

The resulting slurry was dried in a freeze dryer in order to obtain the precursors of KNN powders that were then calcined at 700°C for 9 h. Afterwards, the powders were again planetary-milled at 400 rpm for 120 min, and finally freeze-dried. The calcined powders obtained using the two different batches as starting material were named as KNN1C and KNN2C respectively.

KNN pack-powder containing 2 wt.% alkali excess, produced following the same procedure, was used to compensate possible Na and K losses and maintain chemical stoichiometry during the sintering process.

Pellets (ø = 10 mm) were obtained by linearly pressing the powders at 2000 kg/cm^2 and then subjecting the resulting bodies to cold isostatic pressing at 3000 kg/cm^2. The so-obtained pellets were then sintered at 1130°C for 2 h (heating rate 150°C/h), in the presence of KNN pack powder in a sealed alumina crucible. The sintered pellets were then ground and electrodized on both sides by screen printing conductive Ag paste (consolidated at 750°C for 15 min), and finally poled in silicone oil at 120°C for 30 minutes under an applied DC field of 3 kV/mm.

2.2 Powders and discs characterizations

The crystal structure of both the powders (before and after calcination) and the sintered pellets was investigated using a X-ray diffractometer (Smartlab II Rigaku, Japan), at 1°/min scanning rate over the $10° \leq 2\Theta \leq 80°$ range (step 0.020°), using Cu-Kα radiation (λ = 1.5406 Å) at 40 kV and 40 mA. The Rietveld analysis [22-24] of the diffraction patterns of the powders KNN1C and KNN2C has been performed using GSAS-II©(General Structure Analysis System) [25, 26] and VESTA© for crystals 3D visualization [27] software.

The particle size distribution of the calcined powders was measured after 1h sonication using a Mastersizer 3000 (Malvern Panalytical laser diffraction particle analyzer).

The green and sintered density was measured both as the mass-to-geometric volume ratio and by the Archimedes' method. The relative density was then calculated as the ratio of the experimental to the theoretical value (4.517 g/cm^3).

Field Emission Scanning Electron Microscopy (FE-SEM; Carl Zeiss Sigma NTS Gmbh Öberkochen, Germany) and energy dispersive X-ray spectroscopy (EDS, INCA Energy 300, Oxford instruments, UK)

were employed to analyse the powder's morphology and composition. In order to verify the final stoichiometry and investigate the microstructure of the sintered KNN, SEM-EDS analyses were also performed, both on fracture surfaces and polished cross sections thermally etched at 980°C for 15 minutes.

Cumulative grain size distribution curves of the sintered samples were determined by image analysis of SEM micrographs of the polished and thermally etched cross-sections, using the ImageJ software.

The sample's piezoelectric activity was tested at least 24 hours after poling by the piezoresonance method using an HP 4194A (Hewlett Packard, USA) impedance analyser, detecting resonance and anti-resonance frequencies corresponding to local minima and maxima of the impedance curve. Dielectric dispersion and dielectric loss were measured in the 100 Hz–40 MHz range at room temperature using the HP 4194A impedance analyser. The mechanical and piezoelectric parameters were calculated according to the 1986 ASTM Standard on Piezoelectricity.

The d_{33} piezoelectric coefficient was independently measured using a Sinocera S 5865 d_{33}-meter calibrated with a 360 pC/N d_{33} standard sample provided by the manufacturer.

3. Results and discussion

3.1 Planetary milling

Mechanochemical reactions are promoted via energy transfer between milling bodies and the powder being milled. For instance, Santhanam et al. used a discrete element model that made it possible to predict milling conditions of a scaled-up process, illustrating how the high forces developed in such events can dissipate energy as heat or as plastic deformation of the milling tools instead of refining the material being milled [28]. In fact, if the amount of transferred energy and the number of impacts delivered to the reacting powders are high enough, the pure perovskitic phase can be synthesized at room temperature, as shown by Lee et al. [29]. In milder conditions, the milling of the raw materials mixture is a critical step, both to activate the reaction towards the synthesis of the ferroelectric phase before heating [30] and to enhance the sinterability of the reacted powders by tailoring the morphology, i.e. by decreasing the particle size to enhance the driving force [31]. The milling of the KNN powders has been investigated by several groups and has been performed mostly as ball milling or planetary milling obtaining comparable results, with typically longer times needed for the ball milling treatment. Here planetary milling was selected as a mean to

significantly enhance the reactivity of the starting raw materials mixture (preliminary mechanical activation) [32] and to improve the morphology of the powders before sintering. The amount of energy involved in both grinding treatments was calculated for both KNN1 and KNN2 batches.

The main problem in creating a coherent mathematical model comes from the numerous milling parameters that describe the energetics of the high-energy milling process [33]. Burgio *et al.* derived kinematic equations to describe the velocity and the acceleration of the balls in the planetary mill's vial considering the operative milling parameters [34]. Ball-impact energy (ΔEb in J/hit) and impact frequency (v_t in s^{-1}) can be calculated using Eq. (1) and (2).

$$|\Delta E_b| = \frac{1}{2} m_b W_V^2 \left(R_V - \frac{d_b}{2}\right)\left[\left(R_V - \frac{d_b}{2}\right)\left(\frac{W_V}{W_p}\right) + 2R_p\left(\frac{W_p}{W_V}\right)\right] \quad (1)$$

$$|v_t| = N_b K (W_V - W_p) \quad (2)$$

In Eq (1) and (2), ρ_b is the density and d_b the diameter of the balls, W_p the rotational frequency of the supporting disk, W_v the rotational frequency of the vial, D_v the diameter of the vial, R_p the distance between the rotational axes and N_b the number of balls. The value of K is a dimensionless constant depending on the geometry of the mill and on the ball diameter.

Magini *et al.* showed that the K value can be estimated to be 1.5 for ball diameters around 10 mm; therefore in this work a value of 0.3 has been used for the calculations, considering a milling media diameter equal to 2 mm [35, 36]. Furthermore, it is necessary to take into account the mutual hindering effect of the balls during the milling process, which decreases the ball-impact energy in the system. For this purpose, a hindrance factor Φ_b was introduced into the equations in order to obtain a corrected ball-impact energy (ΔE_b^* in J/hit) as shown in Eq (3).

$$\Delta E_b^* = \Phi_b |\Delta E_b| \quad (3)$$

Usually, Φ_b is assigned the value 0 when the vial is filled with balls, and 1 when no balls or a single ball are present. In this work, Φ_b was calculated as the ratio of the volume occupied by the powder, balls and water to the volume of the jar. In this respect, a defined value of the hindrance factor in each milling process

could be assigned, obtaining values ranging between 0.1 and 0.5. Finally, the ball-impact energy has been normalized to powder mass (m_p). Normalized ball impact energy times milling time *t* yields the cumulative kinetic energy released into the system (ΔE_{cum}, in J/g), as shown in Eq. (4).

$$\Delta E_{cum} = \frac{\Delta E_b^* v_t t}{m_p} \quad (4)$$

Table 1 shows the milling parameters used for the activation of the two different batches of KNN powders. In the first batch (KNN1), the calculated cumulative kinetic energy (ΔE_{cum}) threshold is about 10 J/g before the calcination process, while for the second batch it is six times lower with respect to the previous one. Additionally, it is worth noticing how – at the same ball impact energy ΔE_b provided to the system - the hindrance factor Φ_b is the main parameter affecting the energy released to the system as predicted by the abovementioned equations.

Table 1. Planetary milling conditions for KNN precursors batches (KNN1 and KNN2) and their corresponding calcined powders (KNN1C and KNN2C): rotational speed, hindrance factor (Φ_b), ball impact energy (ΔE_b), corrected ball impact energy (ΔE_b*) and kinetic energy released into the system (ΔE_{cum}).

Powder	Rotational speed	Powder mass	Φb	ΔEb	ΔEb*	ΔEcum
	(rpm)	(g)	/	(μJ/hit)	(μJ/hit)	(J/g)
KNN1	600	34	0.51	8.9	4.5	12.9
KNN1C	400	30	0.54	4.0	2.2	5.6
KNN2	600	79	0.12	8.9	1.0	2.2
KNN2C	400	70	0.22	4.0	0.9	1.7

**Jar vial volume 250 ml and diameter 7.5 cm; 2 mm-diameter zirconia balls with density of 6.05 g/cm³; distance between the rotational axes of the supporting disc and the milling vial, R_p = 12 cm; in both experiments , the vial rotational speed W_v is twice the rotational speed of the supporting disc ($W_v = 2W_p$). The milling time was 100 min before and 120 min after calcination, respectively. Ball-impact energy and ball-impact frequency are calculated according to the Burgio* et al *method [34].*

3.2 Powder characterization

The effect of the cumulative kinetic energy on the precursor's activation was evaluated by XRD and SEM-EDS analyses. In Figure 1 the XRD patterns of the as-mixed raw materials and after first planetary milling of KNN1 and KNN2 powders are shown. As expected, three phases are present, i.e. the starting raw

materials, Nb_2O_5 (COD DB card number #1528678), Na_2CO_3 (COD DB card number #1527606) and K_2CO_3 (COD DB card number #9009645). The enlargement of the peaks after milling provides evidence of the milling effect on the phase's crystallite size: for Nb_2O_5 it reduces from 17.64 nm in the raw mixture to 13.65 nm in the KNN2 and 9.73 nm in KNN1, respectively. The milling energy released in the system is in fact not sufficient to promote directly the synthesis of KNN phase. However, in both KNN1 and KNN2 XRD patterns at low angle (2θ = 10.65°) a new phase of potassium niobate ($K_4Nb_6O_{17}$ COD DB card number #1001842) was detected. Besides the reduction of the grain size, some differences between the two activated batches can be observed in the XRD pattern. In fact, KNN2 shows more intense $K_4Nb_6O_{17}$ peaks in the 2θ range = 22.5°-27.5°, which could be taken as evidence of incipient reactions among the finer particles, the extent of which is difficult to quantify. The presence of this intermediate phase based on potassium niobate appears in a work by Chen et al. [15] too. Normally, the calcination temperature is selected in the 700–950 °C range, which allows obtaining the perovskite phase while avoiding formation of the liquid K-rich phase, thus increasing the density of KNN ceramics; here the lower temperature was applied.

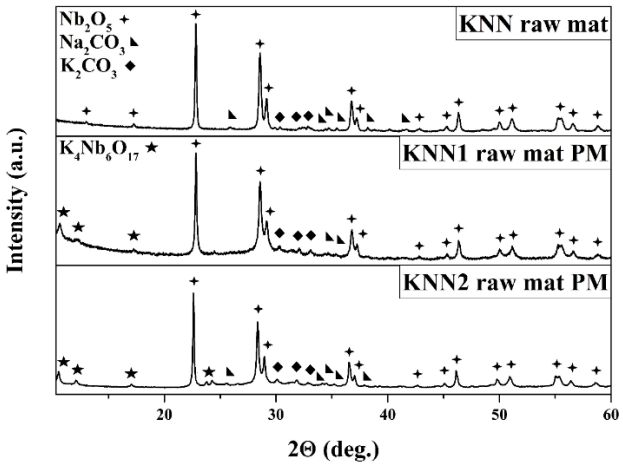

Figure 1. XRD analysis of reactants after mixing of raw materials (KNN raw mat) and after first planetary milling for the KNN1 batch (KNN1 raw mat PM) and for the KNN2 batch (KNN2 raw mat PM).

The influence of the mechanical activation of the precursor's powder on the formation of the perovskite KNN phase is shown in the XRD patterns recorded for the calcined and milled powders, obtained from the two different batches (Figure 2). In Figure 2a, the characteristic peaks of $K_{0.5}Na_{0.5}NbO_3$ are shown for the KNN1C calcined powder while for KNN2C calcined powder a non-stoichiometric perovskitic phase is present along with peaks attributable to trace amounts of niobates by-products (Figure 2b).

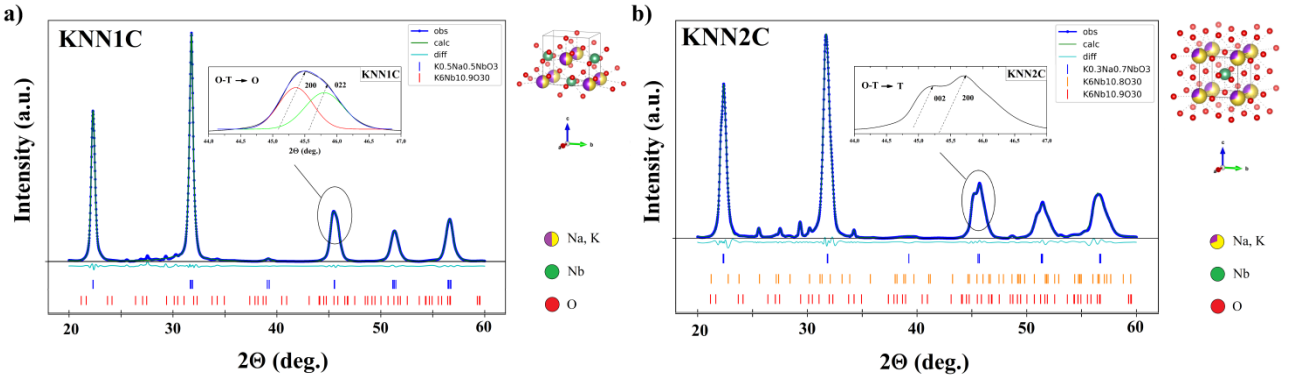

Figure 2. XRD analysis of KNN1C (a) and KNN2C (b) calcined powders with their characteristic peaks in the 44-47° 2Θ narrow range and 3D crystal structure.

Table 2 shows Rietveld refinement performed on KNN1C and KNN2C powders in order to confirm different stoichiometry and thus different "activation" before the calcination process.

Table 2. Lattice cell parameters, space group and phases weight fraction (%) in the two different activated batch (KNN1C and KNN2C) derived by the Rietveld refinement using GSAS-II software.

Powder	***a* (Å)**	***b* (Å)**	***c* (Å)**	**Space group**	**$K_{0.5}Na_{0.5}NbO_3$ (#2300499)**	**$K_{0.3}Na_{0.7}NbO_3$ (#2104294)**	**$K_6Nb_{10.9}O_{30}$ (#4030854)**	**$K_6Nb_{10.8}O_{30}$ (#8101301)**
KNN1C	3.981537	5.645365	5.607094	*A m m 2*	>99.5%	-	<0.5%	-
KNN2C	3.968676	3.968676	3.976875	*P 4 m m*	-	93.5%	2%	4.5%

KNN1C powder is a pure KNN phase (K/Na 1:1, COD DB card number #2300499) with non-centrosymmetric A-centered orthorhombic lattice structure (R_w = 5.85%) and crystallite size 10.47 nm. However, a secondary phase of potassium niobate ($K_6Nb_{10.9}O_{30}$ COD DB card number #4030854) is still present in trace. On the other hand, KNN2C powder is mainly a non-stoichiometric $K_{0.3}Na_{0.7}NbO_3$ KNN phase (COD DB card number #2104294) with a non-centrosymmetric primitive tetragonal lattice structure (R_w = 5.16%), 9.75 nm crystallite size, and the presence of two different potassium niobates. In fact, not properly activated KNN2C powder shows a mixture of two potassium by-products: $K_6Nb_{10.9}O_{30}$ (COD DB card number #4030854, Rietveld refinement *P 4/m b m* with *a* = 11.847434 Å and *c* = 4.104022 Å), and $K_6Nb_{10.8}O_{30}$ (COD DB card number #8101301, Rietveld refinement *P 4/m b m* with *a* = 11.821307 Å and *c* = 3.898719 Å), also confirmed by the calculated lattice constants published in the literature [37]. The niobium-rich phases in KNN2C can be formed either as a consequence of the low thermal budget [38] expressed as

low ΔE_{cum}(kJ/g) value as determined in accordance with our model, resulting in not well-activated precursors, or as a result of alkali-loss during the calcination process at high temperatures [13] favored by the non-stoichiometry of the prevailing (main) phase. Moreover, this kind of niobium-oxide rich phase could be related to the CO_2-enriched atmosphere during calcination, which most probably shifts the equilibrium of the KNN synthesis reaction towards the reagents side [39]. However, since those powders have been calcined in the same configuration (similar powder/container volume ratio in air atmosphere), suggesting comparable alkali loss, it can be inferred that the KNN final stoichiometry is mostly ascribable to different energy activation of the precursors prior to the calcination process.

Being milling conditions and calcination temperature (700°C) the same, these results show how a different jar hindrance factor, i.e. a different released cumulative kinetic energy from scaling the batch up, leads to a different product. The reported results demonstrate that mechanochemical activation occurred during the high-energy ball milling process, inducing the predominant formation of the KNN phase in both batches. However, in the case of KNN2C the amount of energy available for activation was not enough to promote correct phase stoichiometry and avoid by-products.

The particle morphology of powders after calcination and second milling was observed by SEM analysis and is shown in Figure 3 and 4. Both batches show agglomerate powder particles. In detail, KNN2C powder feature bigger platelets geometry as compared to KNN1C, and smaller satellite particles. Indeed, KNN2C powder displays evident particle inhomogeneity (Figure 4b) due to the presence of intermediate and undesired phases. Those particles are most likely associated with the multi-niobates, as detected by XRD (Figure 2b). On the other hand, KNN1C powder appears more homogenous and EDX analysis confirmed the correct KNN stoichiometry (atomic %: 60.1 ± 0.3 O, 9.8 ± 0.2 Na, 10.1 ± 0.2 K, 20.2 ± 0.3 Nb).

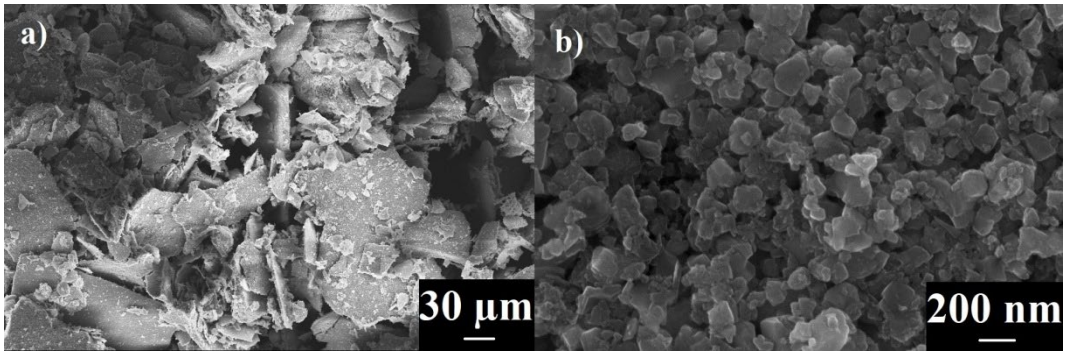

Figure 3. SEM micrographs of milled KNN1C powder at low (a) and higher (b) magnification.

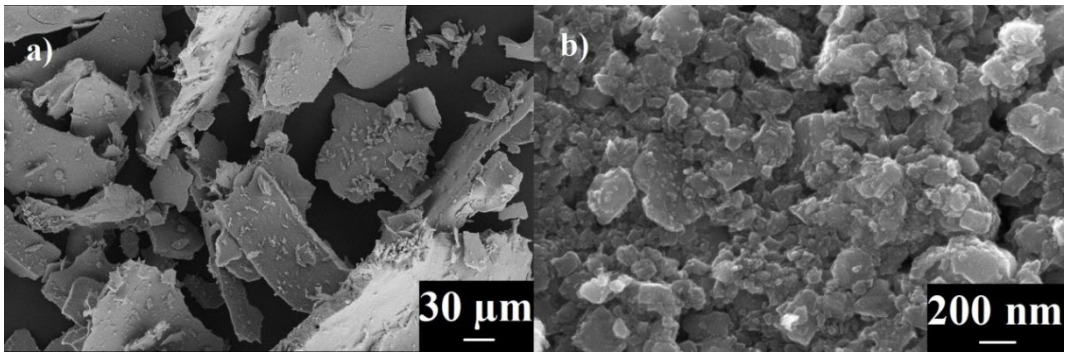

Figure 4. SEM micrographs of milled KNN2C powder at low (a) and higher (b) magnification.

Additional evidence is shown in Fig. 5, where a detail of the KNN2C powder can be seen, evidencing how the inhomogeneous chemical composition with respect the KNN1C powder, influences the EDX analysis of the sample. Indeed, uncommon crystal geometries are clearly observable in the powder, probably ascribable to undesired phases.

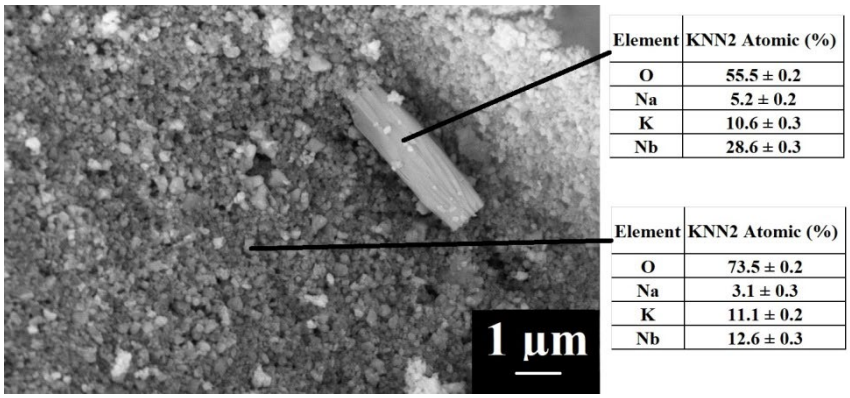

Element	KNN2 Atomic (%)
O	55.5 ± 0.2
Na	5.2 ± 0.2
K	10.6 ± 0.3
Nb	28.6 ± 0.3

Element	KNN2 Atomic (%)
O	73.5 ± 0.2
Na	3.1 ± 0.3
K	11.1 ± 0.2
Nb	12.6 ± 0.3

Figure 5. SEM micrograph of milled KNN2C powder at high magnification with EDX spots analysis.

In Figure 6, the comparison of the corresponding particle size distribution profiles reveals that the apparent large agglomerates detected by the SEM analysis are disintegrated by ultra-sonication before analysis. In fact, both batches have same D90 (≈12.5 µm) but very different particles distribution, which in the case of KNN2C is bimodal. It is possible to note that the state of agglomeration of the largest particles is the same for both batches. Nevertheless, even if the D90 values are the same, in scaled-up batches different milling conditions lead to a dissimilar volume density ratio between small and large particles. Hence, KNN2C powder is much finer, with prevailing submicronic particle size and almost one order of magnitude difference in the D50 and D10 values in comparison to KNN1C. This behavior might be related to the more

reacted raw material mixture of KNN1 that promotes the KNN phase formation at an earlier stage of the calcination process with respect to KNN2, thus increasing powder aggregation during the quite long dwell time (9h). Finally, considering that the milling and calcination processes were performed in the same conditions apart from a scale-up factor, these results demonstrate that the hindrance factor Φ_b is a key-parameter for the solid-state synthesis, affecting the perovskite phase formation and particle size and morphology.

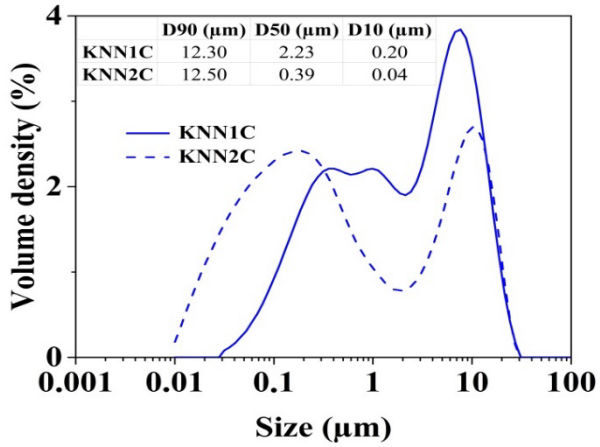

Figure 6. Particle size distribution of the calcined KNN powder batches reported as volume density distribution.

3.3 Sintered samples

The properties of KNN ceramics produced from the two different powder batches were evaluated using XRD. In Figure 7, the XRD patterns of the sintered pellets are shown. Both samples display peaks between 45° and 47°, typical of the orthorhombic phase (ratio of relative intensities of (220)o and (002)o for both samples is close to 2:1) and impurities of potassium niobates. Only in KNN2C pellets niobium oxide peaks were observed. Specifically, a main secondary phase of $K_6Nb_{10.9}O_{30}$ (COD DB card number #4030854) is present like in the starting KNN2C powder; however, in the KNN1C pellet trace amounts of another potassium secondary phase ($K_{0.71}NbO_{3.5}$ COD DB card number #2104829) appear. These data further confirm the critical role of the powder's activation on the nature of residual impurities/secondary phases in the final KNN ceramic.

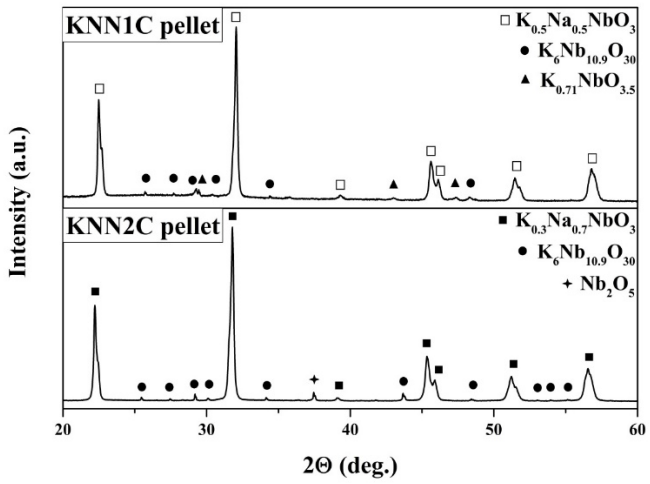

Figure 7. XRD analysis of KNN1C and KNN2C sintered pellets.

On the other hand, SEM-EDX analyses (Table 3) performed on the polished fracture surface of the corresponding KNN ceramics show that the initial overall stoichiometry of the starting powders is preserved after the sintering treatment, without any detectable difference between the two powder batches. Only a slight deficiency of potassium has been detected for the sintered pellets from both batches.

Table 3. SEM-EDX analysis of KNN1C and KNN2C sintered pellets.

Element	Theoretical Atomic (%)	KNN1C Atomic (%)	KNN2C Atomic (%)
O	60	63.3 ± 0.3	63.0 ± 0.6
Na	10	9.7 ± 0.2	9.5 ± 0.2
K	10	8.1 ± 0.2	8.0 ± 0.2
Nb	20	19.0 ± 0.3	19.4 ± 0.3

The microstructure of the KNN ceramics is strongly affected by the different activation of the powders. Fracture surfaces SEM micrographs of KNN1C and KNN2C sintered pellets are shown in Figure 8. For both samples, the typical microstructure with cuboidal grains of KNN-based ceramics was observed. Moreover, it is evident that a strong mechanical activation of the starting powders is effective to prevent abnormal grain growth and the consequent undesired bimodal microstructure generally obtained in sintered KNN produced from powder synthesized by solid-state reaction [9]. This result is also confirmed by the

SEM images of the polished and thermally etched surfaces, where the grain size cumulative distributions of the KNN1C and KNN2C sintered pellets were extrapolated (Fig. 9). The microstructures are constituted by sub-micronic cubic-shaped grains with D50 values of 0.24 and 0.36 μm for KNN1C and KNN2C ceramics respectively. The reduced grain size by using a high energy-ball milling process was shown also by Chen at al. [15].

However, it is very interesting to notice how the microstructure of the KNN ceramics is strongly affected by the differently activated powders. In particular, the more energy-activated KNN1 powder leads to a finer microstructure (Fig. 8a) with evident residual porosity (relative density achieved 90.9 ± 1.9 %), while the microstructure of KNN2 ceramic is constituted by a glassy-like microstructure in which the typical cubic grains are incorporated (Fig. 8b). This result is in accordance with a more densified microstructure (relative density achieved 93.3 ± 0.2 %) and larger grain size respect to the KNN1 sintered pellets, as shown by the grain size cumulative distribution curves in Figure 9.

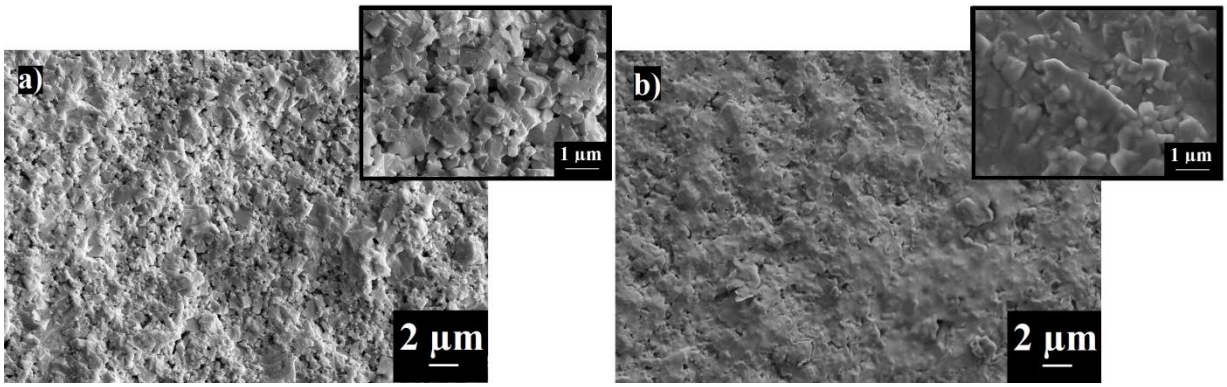

Figure 8. SEM micrographs of the fracture surfaces of KNN1C (a) and KNN2C (b) sintered pellets.

This different behavior could be ascribable to either the significantly finer size of the calcined KNN2 powder that enhances its sinterability, and to the different nature and amount of the alkali-based impurities/secondary phases in the less-activated powder batch (KNN2). In fact, impurities and secondary phases are well known to strongly affect the grain-boundary mobility and, as a consequence, the sintering process and the final microstructure [9-11].

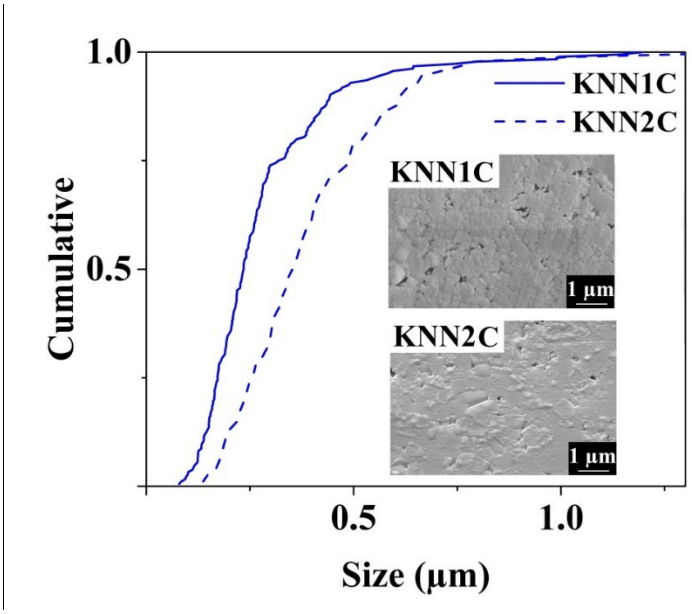

Figure 9. Grain size distribution and SEM micrographs of the polished and thermally etched surface of the sintered pellets from KNN1C (a) and KNN2C (b) batches.

The main results from piezoelectric and dielectric characterizations of the sintered pellets from the two batches are shown in Table 4. They reflect the above considerations; in fact, even though samples from the KNN1 batch are less dense than those from the KNN2 ones, they show significantly better piezoelectric response, i.e. higher k_p, d_{31} and d_{33}. Taking into account that porosity negatively affects the piezoelectric constants, it can be deduced that thorough control of the intermediate phases and morphology is a critical step as well as the optimization of the densification conditions. Mechanical activation is a means to enhance the performance of the material, but an accurate control of every processing parameter is required when scaling up the production. Piezoelectric constants values confirmed once more the crucial role of powders activation, leading to poor d_{33} performance in case of not adequately activated KNN2 powder.

Table 4. Piezoelectric constants of the pellets produced with KNN1C and KNN2C powders. For each powder batch, two pellets were produced at least, herein averaged values are shown.

Sample	ρ	k_p	$-k_{31}$	$-d_{31}$	d_{33}	$-g_{31}$	$-g_{33}$	s_{11}^E	Q_m	σ^E	v_1^E	Z_a
	g/cm^3	/	/	$10^{-12}m/V$		$10^{-3}Vm/N$		$10^{-12}m^2/N$	/	/	m/s	/
KNN1C	4.101	**0.28**	0.162	**57**	**97**	5.33	8.98	**11.7**	26	0.32	**4570**	**18.8**
KNN2C	4.206	**0.22**	0.126	**37**	**65**	5.26	9.77	**12.2**	34	0.33	**4465**	**18.4**

Finally, our results are compared in Table 5 with those reported in the most significant papers on KNN produced by using planetary milling to grind the starting precursors powders mixture (Nb_2O_5, Na_2CO_3 and K_2CO_3).

Table 5. Comparison of various non-doped KNN ceramics synthesized by planetary milling.

Raw materials milling	**Calcination conditions**	**Milling of calcined powder**	**Cold consolidation**	**Densification**	**Density (g/cm^3)**	**d_{33} (pC/N)**	**Reference**
Planetary milling 300-600 rpm 20-360 min	700°C / 9h	Ball milled + freeze drying	Pressed with binder, CIP (200 MPa) to 10mm disk	1120-1140°C / 2h	4.28-4.33	78	[15]
Ball milling / 20h	900°C / 4h	Planetary milling 100-400 rpm 20 h	Pressed with binder (PVA) to 10mm disk	1110°C / 1h	4.08-4.31	83-114	[20]
High energy milling / 6-32h	550°C / 2h	-	-	1100°C / 2h	4.20	95	[21]
Planetary milling 165 rpm / 8h	500-1000°C / 6h	-	-	-	4.39-4.49	-	[40]
Planetary milling / 4h in acetone	2x800°C / 4h	Planetary milling / 4h in acetone	CIP at 200MPa	1120°C / 2h	3.91-4.21	-	[41]
Planetary milling 175 rpm / 4h in acetone	800°C / 4h and 750°C for 4h	Planetary milling 175 rpm / 4h in acetone	Pressed (50 MPa) and CIP (200 MPa)	1100°C / 2h	4.32	88	[42]
Planetary milling / 24h in ethanol	950°C / 3h	Planetary milling / 6-48h in ethanol	Uniaxial pressing to 10 mm disk	1020-1130°C / 4h	4.35-4.44	92-117	[43]
Planetary milling 600 rpm / 100 min	700°C for 9h	Planetary milling 400 rpm / 120 min Freeze drying	CIP (300 MPa) to 10mm disk	1130°C / 2 h (PACK)	4.21- 4.10	65-97	This paper

The comparison shows a variability of the material's properties in terms of final density and representative piezoelectric response (d_{33}). Despite quite similar processing conditions, significantly different properties show that further studies are needed to define precise preparation protocols aimed at improving the reproducibility of the final properties of the material and eventually designing the most appropriate industrial-scale process. In particular, a finer control of crucial parameters like mechanical energy supply during grinding and thermal energy delivery during calcination and densification are key steps worth focusing on.

4. Conclusions

KNN ceramics were successfully synthesized by the mechanochemical activation-assisted method, and the scaled-up powder solid-state reaction synthesis process was studied in order to understand the effect of powder milling. In summary, it was shown that controlling the hindrance factor of the jar used for the synthesis ($\Phi_b > 0.5$) makes it possible to achieve proper stoichiometry during the KNN-phase formation. Besides, compared to the conventional slow ball milling, the planetary milling process allows reducing both KNN powders production time and calcination temperature (700°C). Our results suggest that mechanochemical activation-assisted synthesis method is a promising strategy for industrial scale up to produce KNN-based ceramics under mild conditions, achieving good piezoelectric properties (d_{33} = 97 pC/N) that could be further improved by using doping and achieving higher final density.

Acknowledgements

The research was carried out within the framework of the Joint Research Laboratory between Politecnico di Milano and STMicroelectronics with the aim at developing innovative MEMS devices and technological processes. Authors would like to acknowledge the "Functional Sintered Materials (Funtasma)" Interdepartmental Laboratory of Politecnico di Milano, where this research activity was partially developed. Finally, RB acknowledges the support given by Claudio Capiani for the preparation of the samples during his stage at CNR-ISTEC.

Conflict of Interest

The authors declare there is no conflict of interest.

References

[1] Y. Saito, H. Takao, T. Tani, T. Nonoyama, K. Takatori, T. Homma, T. Nagaya, M. Nakamura, Lead-free piezoceramics, Nature. 432 (2004) 84–87. https://doi.org/10.1038/nature03028.

[2] K. Wang, B. Malič, J. Wu, Shifting the phase boundary: Potassium sodium niobate derivates, MRS Bull. 43 (2018) 607–611. https://doi.org/10.1557/mrs.2018.178.

[3] T.R. Shrout, S.J. Zhang, Lead-free piezoelectric ceramics: Alternatives for PZT?, J. Electroceramics. 19 (2007) 111–124. https://doi.org/10.1007/s10832-007-9047-0.

[4] P.K. Panda, B. Sahoo, PZT to lead free piezo ceramics: A review, Ferroelectrics. 474 (2015) 128–143. https://doi.org/10.1080/00150193.2015.997146.

[5] J.F. Li, K. Wang, F.Y. Zhu, L.Q. Cheng, F.Z. Yao, (K,Na)NbO_3-based lead-free piezoceramics: Fundamental aspects, processing technologies, and remaining challenges, J. Am. Ceram. Soc. 96 (2013) 3677–3696. https://doi.org/10.1111/jace.12715.

[6] J. Wu, D. Xiao, J. Zhu, Potassium-sodium niobate lead-free piezoelectric materials: Past, present, and future of phase boundaries, Chem. Rev. 115 (2015) 2559–2595. https://doi.org/10.1021/cr5006809.

[7] A. Chauhan, R. Vaish, C. Bowen, Piezoelectric material selection for ultrasonic transducer and actuator applications, Proc. Inst. Mech. Eng. Part L J. Mater. Des. Appl. (2015) 3–12. https://doi.org/10.1177/1464420713493591.

[8] T. Shao, H. Du, H. Ma, S. Qu, J. Wang, J. Wang, X. Wei, Z. Xu, Potassium–sodium niobate based lead-free ceramics: novel electrical energy storage materials, J. Mater. Chem. A (2017) 554-563. https://doi.org/10.1039/C6TA07803F

[9] B. Malič, J. Koruza, J. Hreščak, J. Bernard, K. Wang, J.G. Fisher, A. Benčan, Sintering of lead-free piezoelectric sodium potassium niobate ceramics, Materials (Basel). 8 (2015) 8117–8146. https://doi.org/10.3390/ma8125449.

[10] M. Kosec, B. Malič, A. Benčan, T. Rojac, J. Tellier, Alkaline niobate-based piezoceramics: Crystal structure, synthesis, sintering and microstructure, Funct. Mater. Lett. 3 (2010) 15–18. https://doi.org/10.1142/S1793604710000865.

[11] J. Acker, H. Kungl, M.J. Hoffmann, Influence of alkaline and niobium excess on sintering and microstructure of sodium-potassium niobate $(K_{0.5}Na_{0.5})NbO_3$, J. Am. Ceram. Soc. 93 (2010) 1270–1281. https://doi.org/10.1111/j.1551-2916.2010.03578.x.

[12] N.M. Hagh, B. Jadidian, A. Safari, Property-processing relationship in lead-free (K Na Li)NbO_3-solid solution system, J. Electroceramics. 18 (2007) 339–346. https://doi.org/10.1007/s10832-007-9171-x.

[13] B. Malic, D. Jenko, J. Holc, M. Hrovat, M. Kosec, Synthesis of sodium potassium niobate: A diffusion couples study, J. Am. Ceram. Soc. 91 (2008) 1916–1922. https://doi.org/10.1111/j.1551-2916.2008.02376.x.

[14] Y. Wang, D. Damjanovic, N. Klein, E. Hollenstein, N. Setter, Compositional inhomogeneity in Li- and Ta-modified (K, Na)NbO_3 ceramics, J. Am. Ceram. Soc. 90 (2007) 3485–3489. https://doi.org/10.1111/j.1551-2916.2007.01962.x.

[15] B. Chen, P. Liang, D. Wu, X. Zhao, X. Qiao, Z. Peng, L. Wei, X. Chao, Z. Yang, High-efficiency synthesis of high-performance $K_{0.5}Na_{0.5}NbO_3$ ceramics, Powder Technol. 346 (2019) 248–255. https://doi.org/10.1016/j.powtec.2019.01.039.

[16] T. Rojac, M. Kosec, B. Malič, J. Holc, Mechanochemical synthesis of $NaNbO_3$, $KNbO_3$ and $K_{0.5}Na_{0.5}NbO_3$, Sci. Sinter. 37 (2005) 61–67. https://doi.org/10.2298/SOS0501061R.

[17] T. Rojac, M. Kosec, B. Malič, J. Holc, The application of a milling map in the mechanochemical synthesis of ceramic oxides, J. Eur. Ceram. Soc. 26 (2006) 3711–3716. https://doi.org/10.1016/j.jeurceramsoc.2005.11.013.

[18] T. Rojac, M. Kosec, B. Malič, J. Holc, The mechanochemical synthesis of $NaNbO_3$ using different ball-impact energies, J. Am. Ceram. Soc. 91 (2008) 1559–1565. https://doi.org/10.1111/j.1551-2916.2008.02315.x.

[19] M. Abdellahi, M. Bahmanpour, Rapid synthesis of nanopowders in high energy ball milling; optimization of milling parameters, Ceram. Int. 41 (2015) 1631–1639. https://doi.org/10.1016/j.ceramint.2014.09.101.

[20] C. Jiten, M. Rawat, A. Bhattacharya, K.C. Singh, $(Na_{0.5}K_{0.5})NbO_3$ nanocrystalline powders produced by high energy ball milling and corresponding ceramics, Mater. Res. Bull. 90 (2017) 162–169. https://doi.org/10.1016/j.materresbull.2017.02.031.

[21] R. Singh, P.K. Patro, A.R. Kulkarni, C.S. Harendranath, Synthesis of nano-crystalline potassium sodium niobate ceramic using mechanochemical activation, Ceram. Int. 40 (2014) 10641–10647. https://doi.org/10.1016/j.ceramint.2014.03.047.

[22] H.M. Rietveld, Line profiles of neutron powder-diffraction peaks for structure refinement, Acta Crystallogr. 22 (1967) 151–152. https://doi.org/10.1107/s0365110x67000234.

[23] J.O. Thomas, G. Malmros, Least-squares structure refinement based on profile analysis of powder film intensity data measured on an automatic mircodensitometer, J. Appl. Crystallogr. 10 (1977) 7–11. https://doi.org/10.1107/S0021889877012680

[24] L.B. Mccusker, R.B. Von Dreele, D.E. Cox, D. Louër, P. Scardi, Rietveld refinement guidelines, J. Appl. Crystallogr. 32 (1999) 36–50. https://doi.org/10.1107/S0021889898009856.

[25] General Structure Analysis System-II by Robert B. Von Dreele and Brian H. Toby, Argonne National Laboratory (C), 2010.

[26] B.H. Toby, R.B. Von Dreele, GSAS-II: The genesis of a modern open-source all-purpose crystallography software package, J. Appl. Crystallogr. 46 (2013) 544–549. https://doi.org/10.1107/S0021889813003531.

[27] K. Momma, F. Izumi, VESTA 3 for three-dimensional visualization of crystal, volumetric and morphology data, J. Appl. Crystallogr. 44 (2011) 1272–1276. https://doi.org/10.1107/S0021889811038970.

[28] P.R. Santhanam, E.L. Dreizin, Predicting conditions for scaled-up manufacturing of materials prepared by ball milling, Powder Technol. 221 (2012) 403–411. https://doi.org/10.1016/j.powtec.2012.01.037.

[29] G.J. Lee, E.K. Park, S.A. Yang, J.J. Park, S.D. Bu, M.K. Lee, Rapid and direct synthesis of complex perovskite oxides through a highly energetic planetary milling, Sci. Rep. 7 (2017) 1–11. https://doi.org/10.1038/srep46241.

[30] P. Baláž, M. Achimovicová, M. Baláž, P. Billik, C.Z. Zara, J.M. Criado, F. Delogu, E. Dutková, E. Gaffet, F.J. Gotor, R. Kumar, I. Mitov, T. Rojac, M. Senna, A. Streletskii, W.C. Krystyna, Hallmarks of mechanochemistry: From nanoparticles to technology, Chem. Soc. Rev. 42 (2013) 7571–7637. https://doi.org/10.1039/c3cs35468g.

[31] W.D. Kingery, H.K. Bowen, D.R. Uhlmann, Introduction to Ceramics, second ed., Wiley-Interscience, New York, NY, USA, 1976.

[32] A.S. Rogachev, Mechanical activation of heterogeneous exothermic reactions in powder mixtures, Russ. Chem. Rev. 88 (2019) 875–900. https://doi.org/10.1070/rcr4884.

[33] M. Abdellaoui, E. Gaffet, The physics of mechanical alloying in a planetary ball mill: Mathematical treatment, Acta Metall. Mater. 43 (1995) 1087–1098. https://doi.org/10.1016/0956-7151(95)92625-7.

[34] N. Burgio, A. Iasonna, M. Magini, S. Martelli, F. Padella, Mechanical alloying of the Fe-Zr system. Correlation between input energy and end products, Nuovo Cim. D. 13 (1991) 459–476. https://doi.org/10.1007/BF02452130.

[35] M. Magini, A. Iasonna, Energy Transfer in Mechanical Alloying (Overview), Mater. Trans. JIM. 36 (1995) 123–133. https://doi.org/10.2320/matertrans1989.36.123.

[36] M. Magini, A. Iasonna, F. Padella, Ball milling: An experimental support to the energy transfer evaluated by the collision model, Scr. Mater. 34 (1996) 13–19. https://doi.org/10.1016/1359-6462(95)00465-3.

[37] E. Irle, R. Blachnik, B. Gather, The phase diagrams of Na_2O and K_2O with Nb_2O_5 and the ternary system Nb_2O_5-Na2O-Yb_2O_3, Thermochim. Acta. 179 (1991) 157–169. https://doi.org/10.1016/0040-6031(91)80344-I.

[38] B.Y. Kim, T.G. Seong, I.T. Seo, M.S. Jang, S. Nahm, J.Y. Kang, S.J. Yoon, Effects of annealing atmosphere on the structural and electrical properties of $(Na_{0.5}K_{0.5})NbO_3$ thin films grown by RF magnetron sputtering, Acta Mater. 60 (2012) 3107–3112. https://doi.org/10.1016/j.actamat.2012.02.015.

[39] A. Popovič, L. Bencze, J. Koruza, B. Malič, Vapour pressure and mixing thermodynamic properties of the KNbO3-NaNbO3 system, RSC Adv. 5 (2015) 76249–76256. https://doi.org/10.1039/c5ra11874c.

[40] M. Feizpour, T. Ebadzadeh, D. Jenko, Synthesis and characterization of lead-free piezoelectric $(K_{0.5}Na_{0.5})NbO_3$powder produced at lower calcination temperatures: A comparative study with a calcination temperature of 850 °C, J. Eur. Ceram. Soc. 36 (2016) 1595–1603. https://doi.org/10.1016/j.jeurceramsoc.2016.01.014.

[41] J. Hreščak, A. Bencan, T. Rojac, B. Malič, The influence of different niobium pentoxide precursors on the solid-state synthesis of potassium sodium niobate, J. Eur. Ceram. Soc. 33 (2013) 3065–3075. https://doi.org/10.1016/j.jeurceramsoc.2013.07.006.

[42] J. Pavlič, B. Malič, T. Rojac, Microstructural, structural, dielectric and piezoelectric properties of potassium sodium niobate thick films, J. Eur. Ceram. Soc. 34 (2014) 285–295. https://doi.org/10.1016/j.jeurceramsoc.2013.09.001.

[43] R. Zuo, J. Rödel, R. Chen, L. Li, Sintering and electrical properties of lead-free $Na_{0.5}K_{0.5}NbO_3$ piezoelectric ceramics, J. Am. Ceram. Soc., 2006: pp. 2010–2015. https://doi.org/10.1111/j.1551-2916.2006.00991.x.

Figure and Table Captions

Figure 1. XRD analysis of reactants after mixing of raw materials (KNN raw mat) and after first planetary milling for the batch 1 (KNN1 raw mat PM) and for the batch 2 (KNN2 raw mat PM).

Figure 2. XRD analysis of KNN1C (a) and KNN2C (b) calcined powders with their characteristic peaks in the 44-47° 2Θ narrow range and 3D crystal structure.

Figure 3. SEM micrographs of milled KNN1C powder at low (a) and higher (b) magnification.

Figure 4. SEM micrographs of milled KNN2C powder at low (a) and higher (b) magnification.

Figure 5. SEM micrograph of milled KNN2C powder at high magnification with EDX spots analysis.

Figure 6. Particle size distribution of the calcined KNN powder batches reported as volume density distribution.

Figure 7. XRD analysis of KNN1C and KNN2C sintered pellets.

Figure 8. SEM micrographs of the fracture surfaces of KNN1C (a) and KNN2C (b) sintered pellets.

Figure 9. Grain size distribution and SEM micrographs of the polished and thermally etched surface of the sintered pellets from KNN1C (a) and KNN2C (b) batches.

Table 1. Planetary milling conditions for KNN precursors batches (KNN1 and KNN2) and their corresponding calcined powders (KNN1C and KNN2C): rotational speed , hindrance factor (Φ_b), ball impact energy (ΔE_b), corrected ball impact energy (ΔE_b*) and kinetic energy released in the system (ΔE_{cum}).

Table 2. SEM-EDX analysis of KNN1C and KNN2C sintered pellets.

Table 3. Piezoelectric constants of the pellets produced with KNN1C and KNN2C powders.

Table 4. Piezoelectric constants of the pellets produced with KNN1C and KNN2C powders. For each powder batch, two pellets were produced at least, herein averaged values are shown.

Table 5. Comparison of various non-doped KNN ceramics synthesized by planetary milling.